INTERNATIONAL JOURNAL FOR NUMERICAL METHODS IN FLUIDS
Int. J. Numer. Meth. Fluids 2007; **53**:371–389
Published online 6 July 2006 in Wiley InterScience (www.interscience.wiley.com). DOI: 10.1002/fld.1283

Using fully implicit conservative statements to close open boundaries passing through recirculations

Masoud Darbandi*,† and Shidvash Vakilipour‡,§

Department of Aerospace Engineering, Sharif University of Technology, Tehran, Iran

SUMMARY

The numerical solution of the fluid flow governing equations requires the implementation of certain boundary conditions at suitable places to make the problem well-posed. Most of numerical strategies exhibit weak performance and obtain inaccurate solutions if the solution domain boundaries are not placed at adequate locations. Unfortunately, many practical fluid flow problems pose difficulty at their boundaries because the required information for solving the PDE's is not available there. On the other hand, large solution domains with known boundary conditions normally need a higher number of mesh nodes, which can increase the computational cost. Such difficulties have motivated the CFD workers to confine the solution domain and solve it using artificial boundaries with unknown flow conditions prevailing there. In this work, we develop a general strategy, which enables the control-volume-based methods to close the outflow boundary at arbitrary locations where the flow conditions are not known prior to the solution. In this regard, we extend suitable conservative statements at the outflow boundary. The derived statements gradually detect the correct boundary conditions at arbitrary boundaries via an implicit procedure using a finite element volume method. The extended statements are validated by solving the truncated benchmark backward-facing step problem. The investigation shows that the downstream boundary can pass through a recirculation zone without deteriorating the accuracy of the solution either in the domain or at its boundaries. The results indicate that the extended formulation is robust enough to be employed in solution domains with unknown boundary conditions. Copyright © 2006 John Wiley & Sons, Ltd.

Received 8 December 2005; Revised 20 April 2006; Accepted 21 April 2006

KEY WORDS: finite volume; finite element; artificial boundary; implicit method; open boundary conditions; backward-facing step

*Correspondence to: Masoud Darbandi, Department of Aerospace Engineering, Sharif University of Technology, Azadi Ave., P.O. Box 11365-8639, Tehran, Iran.
†E-mail: darbandi@sharif.edu
‡E-mail: vakili@mehr.sharif.edu
§Ph.D. Student.

1. INTRODUCTION

During the past several decades, computer simulation models for analysing flow have played an increasingly important role in flow field studies and simulations. In many fluid flow problems, the domain in which we wish to solve the equations is unbounded. To solve the equations numerically, it is necessary to distribute a suitable grid in the domain. To avoid unbounded grid distributions, a standard approach is to place artificial boundaries in the unbounded domain to limit the unbounded physical domain to a confined computational domain. From computational cost perspective, the chosen artificial boundaries should not be placed so far from the domain of interest. Nevertheless, in many fluid flow simulations with unbounded boundaries, a typical remedy is to place suitable artificial boundaries in the domain and apply suitable boundary conditions. The determination of where an artificial boundary can be placed and what kind of boundary conditions are the most suitable ones obviously depend on the objectives of the study. For example, Behr *et al.* [1] and Sohankar *et al.* [2] studied the dependence of the vortex-shedding phenomena on the placement of the lateral and outflow boundaries, respectively. Using different types of boundary conditions, they indicated that the distance between the lateral boundaries and the cylinder beyond and the outflow location should be suitably chosen to avoid inaccuracies in the solution. Consequently, cautious placement of the artificial boundaries is advocated.

One typical approach to treat suitable boundary conditions at artificial boundaries is to use the open boundary conditions, OBCs. The essence of this approach is not to impose Dirichlet boundary condition along the outflow boundary because the fluid may presumably enter or leave the domain through such boundaries. The OBC approach has shown that the solution in the domain can pass through the outflow boundary without undergoing significant distortion and without influencing the interior solution. Griffiths [3] studies one-dimensional convection–diffusion problem and shows that the use of OBCs in finite element methods of degree p is equivalent to imposing the condition that the $(p+1)$st derivative of the dependent variable should vanish in the vicinity of the outflow. In a similar study, Renardy [4] shows the robustness of OBCs at outflow using one-dimensional convection–diffusion problem. Papanastasiou *et al.* [5] apply several types of outflow boundary conditions including essential, natural, and free boundary conditions to solve the backward-facing step problem. They argue that the free boundary condition is equivalent to extending the validity of the weak form of the governing equations to the synthetic outflow instead of replacing them with unknown essential or natural boundary conditions. Sani and Gresho [6] summarize the two mini-symposia on OBCs to find the best OBCs for a small subset of backward-facing step problem. They argue that the contributions obtained probably raised many more questions and doubts than were solved. Then, they identify fuzzy boundary conditions as a new class of OBCs. Keskar and Lyn [7] examine the problem of outflow boundary conditions using spectral domain decomposition method considering two widely utilized set of conditions, i.e. pseudo stress-free conditions and zero normal gradient conditions. Generally speaking, the results provided by such references indicate the great effectiveness of employing OBCs at boundaries with unknown conditions.

From the conservation perspective, Blosch *et al.* [8] showed that the outflow boundary could pass through a recirculation region without adverse effects on solution accuracy. They performed their study on a staggered grid context. They used two inner and outer loops on the pressure correction equation to guarantee a global mass-conserving procedure. Contrary to the staggered grid context, Darbandi and Schneider [9, 10] have developed a pressure-based finite volume method on a collocated grid arrangement using quadrilateral elements. Darbandi *et al.* [11, 12] have already extended the method to use triangular elements. Recently, Darbandi and Naderi [13] extended

DOI: 10.1002/fld

the method to hybrid grid applications. The method has already shown excellent performance and accuracy if the outflow conditions are imposed at proper locations with known boundary conditions. In spite of using a finite volume method, the method does not necessarily guarantee the conservation of either mass or momentum through the cells located on the outflow boundary. Using either Dirichlet or Neumann boundary conditions at outflow, it was found that the bounded physical solution domains with known boundary conditions might not be confined to smaller computational domains with unknown boundary conditions. Following the past attempts described in References [14, 15], we provide a global conservation procedure through the entire solution domain including the outflow boundaries. The performance of the extended formulations is then investigated in solving the truncated backward-facing step problem using non-variational uniform and non-uniform grids. The investigation shows that the extended formulation enables the method to solve the flow fields with arbitrary artificial boundaries. The extended formulation exhibits excellent accuracy comparing with the results of past workers.

2. GOVERNING EQUATIONS

We solve the steady two-dimensional incompressible flow. The governing equations consist of the conservation statements for mass and momentums, which are given by

$$\nabla \cdot (\rho \mathbf{V}) = 0 \tag{1}$$

$$\nabla \cdot (\rho u \mathbf{V}) = -\frac{\partial p}{\partial x} + \nabla \cdot (\mu \nabla u) \tag{2}$$

$$\nabla \cdot (\rho v \mathbf{V}) = -\frac{\partial p}{\partial y} + \nabla \cdot (\mu \nabla v) \tag{3}$$

where $\mathbf{V}$ $(\equiv u\hat{i} + v\hat{j})$, p, ρ, and μ represent velocity, pressure, density, and the fluid viscosity coefficient, respectively.

3. DOMAIN DISCRETIZATION

The solution domain is broken into triangular finite elements. The elements fully cover the solution domain without overlapping. Figure 1 shows a small part of the solution domain. Nodes are located at the triangle vertices, see nodes A, B, and C on triangle ABC. Nodes are the locations of the unknown variables. There is no limit in the number of elements which share one node. For example, there are six triangles which encompass node P, see Figure 1. To utilize the benefits of cell-centred schemes, each element is divided into three quadrilaterals based on its three medians. The medians are demonstrated by dashed line in this figure. The cells are then constructed from the proper assemblage of these quadrilaterals. As it is seen, irrespective of the shape and distribution of the elements, each node is surrounded by a number of quadrilaterals. The proper assemblage of neighbouring quadrilaterals around any non-boundary node generates a cell with polygonal shape. Figure 1 also shows a cell located at the boundary of the domain, which can be an outflow boundary. In this case, the cell centre P_B is exceptionally located on the cell's face.

DOI: 10.1002/fld

4. COMPUTATIONAL MODELLING

To utilize the advantages of both finite element and finite volume methods, the governing equations are initially integrated over an arbitrary cell, e.g. the shaded area in Figure 1. The employment of Gauss divergence theorem to the governing equations results in

$$\int_A \rho \mathbf{V} \cdot \mathrm{d}\mathbf{A} = 0 \tag{4}$$

$$\int_A u(\rho \mathbf{V}) \cdot \mathrm{d}\mathbf{A} = -\int_A p \, \mathrm{d}A_x + \int_A (\mu \nabla u) \cdot \mathrm{d}\mathbf{A} \tag{5}$$

$$\int_A v(\rho \mathbf{V}) \cdot \mathrm{d}\mathbf{A} = -\int_A p \, \mathrm{d}A_y + \int_A (\mu \nabla v) \cdot \mathrm{d}\mathbf{A} \tag{6}$$

The above integrals are evaluated over the faces of each cell. The total area of the faces is indicated by A. The above equations are suitably treated using finite difference stencils and finite element shape functions. In the above expressions, $\mathrm{d}\mathbf{A} = \mathrm{d}A_x \hat{i} - \mathrm{d}A_y \hat{j}$ is a normal outward vector to the edges of cell. In case of a boundary cell, the vector is normal outward to the solution domain boundary for those edges located on the boundary, see Figure 1. Using this definition, the above integrals can be evaluated using summation over the cell faces. This yields

$$\sum_{i=1}^{ns} [\rho(u \, \mathrm{d}A_x + v \, \mathrm{d}A_y)]_i = 0 \tag{7}$$

$$\sum_{i=1}^{ns} [\rho \overline{u} u \, \mathrm{d}A_x + \rho \overline{v} u \, \mathrm{d}A_y]_i = -\sum_{i=1}^{ns} (p \, \mathrm{d}A_x)_i + \sum_{i=1}^{ns} \left[\mu \left(\frac{\partial u}{\partial x} \mathrm{d}A_x + \frac{\partial u}{\partial y} \mathrm{d}A_y \right) \right]_i \tag{8}$$

$$\sum_{i=1}^{ns} [\rho \overline{u} v \, \mathrm{d}A_x + \rho \overline{v} v \, \mathrm{d}A_y]_i = -\sum_{i=1}^{ns} (p \, \mathrm{d}A_y)_i + \sum_{i=1}^{ns} \left[\mu \left(\frac{\partial v}{\partial x} \mathrm{d}A_x + \frac{\partial v}{\partial y} \mathrm{d}A_y \right) \right]_i \tag{9}$$

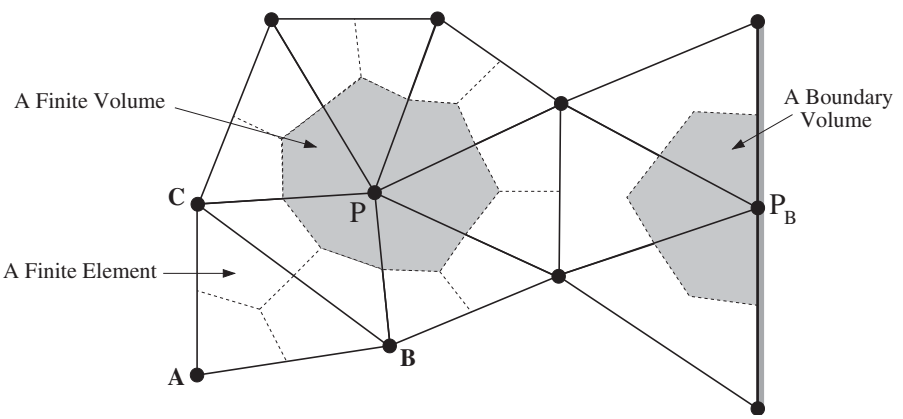

Figure 1. A part of the solution domain illustrating elements, an interior cell, a boundary cell, and many sub-volumes and cell faces.

DOI: 10.1002/fld

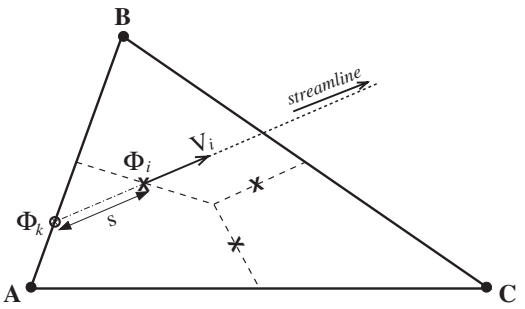

Figure 2. The velocity upwinding strategy within an element.

where i counts the number of cell faces from 1 to ns. There are 12 cell faces around node P in Figure 1. However, this number is 8 for the cell located on the boundary and identified by P_B. To linearize the governing equations, the bar over u and v indicates that these velocity components are approximated from the known magnitudes of the preceding iteration. Such linearization is essential to the nonlinear momentum convection terms. The rest of procedure is to relate the cell face magnitudes (identified by lowercase letters such as u, v and p variables) to the nodal magnitudes (identified by uppercase letters such as U, V and P variables). The nodal variables represent the location of unknown variables in our algorithm. A simple idea for computing the right-hand sides of Equations (8) and (9) is to use the finite element shape functions $N_{j=1,\ldots,3}$. The treatment yields

$$p_i = \sum_{j=1}^{3} (N_j)_i P_j \tag{10}$$

$$\left.\frac{\partial \phi}{\partial z}\right|_i = \sum_{j=1}^{3} \left.\frac{\partial N_j}{\partial z}\right|_i \Phi_j \tag{11}$$

where p_i identifies the magnitude of p at the mid-point of the ith cell face. The subscript j counts the nodes of an element. This element encloses the ith cell face. Additionally, the variable z represents either x or y coordinates and ϕ (and Φ) represents either u (and U) or v (and V) velocity components. As was mentioned earlier, lowercase and uppercase letters are used to represent the cell face and nodal magnitudes, respectively.

The above approximations end the treatment of pressure and diffusion terms at the cell faces. However, more sophisticated expressions are required to treat the convection terms. For example, to mimic the correct physics of the convection, the convection terms should be somehow upwinded. To consider a more inclusive physics of the convection, References [11, 12] extend an upwind-biased scheme (known as a physical influence scheme) within triangular elements. We also follow their scheme. Considering the ith cell face located in triangle ABC, one inclusive expression can be suggested as, see Figure 2,

$$\phi_i = \phi_k + \left(\frac{\partial \phi}{\partial s}\right)_i \Delta S_{ki} \tag{12}$$

DOI: 10.1002/fld

This expression has been written in the streamline direction at mid-point of the ith cell face. The length ΔS_{ki} is a geometry sensitive parameter denoted by s in Figure 2. The subscript k denotes the upstream of the ith cell face. Using Equation (12), we have to determine the gradient of ϕ along the streamline. We try to approximate this gradient using the original governing PDE's. In other words, one inclusive approximation can be derived by writing the revised momentum equations in the streamwise direction. The momentum equations can be revised to

$$\rho V_{\text{tot}} \frac{\partial \phi}{\partial s} = \nabla \cdot (\mu \nabla \phi) + S_\phi \tag{13}$$

where $V_{\text{tot}} = \sqrt{\overline{u}^2 + \overline{v}^2}$ is the total velocity at the cell mid-point and the source term S_ϕ represents either $(-\partial p/\partial x)$ in treating x-momentum equation or $(-\partial p/\partial y)$ in treating y-momentum equation. The substitution of Equation (13) in Equation (12) yields

$$\phi_i = \phi_k + \left[\frac{1}{\rho V_{\text{tot}}} (\nabla \cdot (\mu \nabla \phi) + S_\phi) \right]_i \Delta S_{ki} \tag{14}$$

As observed, the influence of pressure has been considered in calculating the correction term in Equation (12). Using the finite-element tool, Equation (14) is revised to

$$\phi_i = \sum_{j=1}^{3} (N_j)_k \Phi_j + \frac{1}{\rho (V_{\text{tot}})_i} \left(\frac{\sum_{j=1}^{3} (N_j)_i \Phi_j - \phi_i}{L_i^2} - \sum_{j=1}^{3} \left. \frac{\partial N_j}{\partial z} \right|_i P_j \right) \Delta S_{ki} \tag{15}$$

where L_i is an appropriate diffusion length scale [9, 12]. This length can be estimated in a specified triangle by discretizing the diffusion terms in x and y directions using suitable central-difference schemes.

Equation (15) shows that ϕ_i appears on both sides of this equation. Considering a lagged role for $\overline{\phi}$ in the diffusion term, it results in a passive role of diffusion term in the formulations. To shift its role into an active one, we took this term to the left-hand side of Equation (15). A suitable rearrangement of Equation (15) in terms of our major dependent variables, i.e. Φ_j and P_j, finally yields

$$\phi_i = \sum_{j=1}^{3} \alpha_{ij} \Phi_j + \sum_{j=1}^{3} \beta_{ij} P_j + \gamma_i \tag{16}$$

If the subscript i denotes the three cell faces within an element, see Figure 2, α, β, and γ represent two 3×3 matrices, and one 3×1 array of coefficients, respectively. These coefficients measure the weights of pressure and velocity field magnitudes on the cell face velocity magnitude. Equation (16) indicates that ϕ $(\equiv u, v)$ at a cell face can be approximated by the proper assemblage of Φ $(\equiv U, V)$ and P magnitudes at the cell centres of the element, which surrounds that cell face. In fact, this approximation is known as the pressure-weighted streamline upwinding scheme [9–13]. Using a second-order central-difference scheme to discretize the diffusion and pressure terms and a first-order upwind scheme to discretize the convection term in the streamwise direction, the current method is classified into first-order pressure-based methods.

The substitutions of Equations (10), (11) and (16) in Equations (7)–(9) provide three conservative statements for each cell in the domain. If the conservative statements are obtained for all the cells

DOI: 10.1002/fld

in the computational domain, a set of algebraic equations is derived. This set of equations can be compacted into

$$c_{ij}^{pu} U_j + c_{ij}^{pv} V_j + c_{ij}^{pp} P_j = d_i^p \tag{17}$$

$$c_{ij}^{uu} U_j + c_{ij}^{uv} V_j + c_{ij}^{up} P_j = d_i^u \tag{18}$$

$$c_{ij}^{vu} U_j + c_{ij}^{vv} V_j + c_{ij}^{vp} P_j = d_i^v \tag{19}$$

where i and j count the global node numbers, i.e. $i,\ j = 1, \ldots, N\text{node}$. Equations (17)–(19) provide a strong coupling of the velocity and pressure fields within the mass and two momentum equations. It should be noted that the matrix is a diagonal one, which is normally encountered in implicit finite element methods. Therefore, it is strongly sparse and needs sparse solver strategies to solve it efficiently. The coefficients in the global assembled matrix are identified by c. The first letter in its superscripts depicts the type of equation, i.e. p, u, and v indicate continuity, x-momentum, and y-momentum equations, respectively. The second letter in the superscripts indicates of which unknown the coefficient belongs to. The right-hand side vector is shown by d.

Similar to other collocated methods, the current method fully conserves mass and momentum fluxes over each interior cell. However, dissimilar to many other collocated finite volume methods (which normally benefit interpolation schemes such as upwinding, skewed upwinding, quadratic upwind differencing, and hybrid to approximate the cell face velocities), the current method considers a more inclusive statement through using a pressure-weighted streamline upwinding scheme to approximate the cell face velocities. Evidently, the latter statement should be more accurate than the primitive mathematical-based statements.

After deriving an inclusive statement for the cell face velocity components in the interior domain, see Equation (16), the next stage is to use them to close the domain boundaries to achieve global conservations of mass and momentum fluxes through the entire solution domain including its boundaries, and specifically the open boundaries with unknown flow conditions. The outflow boundary is the most ambiguous one among the others because of its unknown flow conditions. The ambiguity is magnified if the outflow is placed at locations where the flow field gradients are large in different directions. Therefore, care should be taken to close such boundaries because of their ambiguous circumstances.

Figure 3 shows the details of a boundary cell located at the outflow boundary of Figure 1. There are three nodes located on the boundary. They are identified using global node numbers of N_b^-, N_b, and N_b^+. Additionally, there are two cell faces above and under node N_b, which need to be considered in our conservation procedure properly. These two faces are labelled by their mid-points, i.e. ip_b^- and ip_b^+. To complete the conservation procedure, the mass and momentum fluxes need to be calculated properly and implemented in the conservation statements at these two faces. It should be reminded that all the fluxes at the interior faces, i.e. $ip_1, \ldots, ip_6$, have been already calculated and included in Equations (17)–(19).

At the first stage, we need to calculate $u_{ip_b}^-$, $v_{ip_b}^-$, $u_{ip_b}^+$, and $v_{ip_b}^+$ to smoothen the conservation procedure. We use finite element shape functions to estimate them from the nodes located at the vertices of their elements. This is achieved using

$$\phi_{ip_b} = \sum_{j=1}^{3} (N_j)_{ip_b} \Phi_j \tag{20}$$

DOI: 10.1002/fld

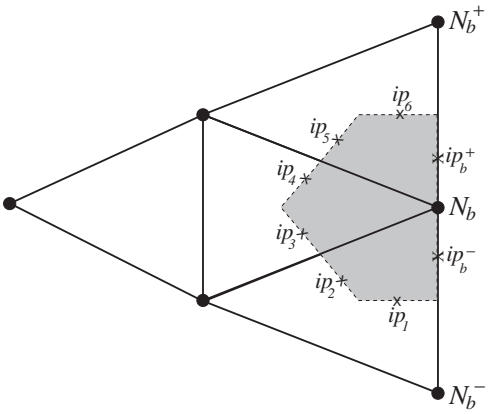

Figure 3. A cell located on the domain boundary showing the contributing nodes (circles) and integration points (crosses) at its faces.

where ϕ (and Φ) represents either u (and U) or v (and V) velocity components. These velocities are used to calculate mass flux at the two boundary faces. If the boundary mass flux is identified by L^{pm}, it is calculated from

$$L^{pm} = \sum_{ip_b=1}^{2} \left[\rho \left(\sum_{j=1}^{3} (N_j)_{ip_b} U_j \, \mathrm{d}A_x + \sum_{j=1}^{3} (N_j)_{ip_b} V_j \, \mathrm{d}A_y \right) \right]_{ip_b} \tag{21}$$

This mass flux is added to the LHS of the continuity equation, i.e. Equation (17). The effect of this assemblage is only appeared in one row of the algebraic set of equations. To be consistent with the interior cells, the velocity calculated in Equation (16) is used to compute the convection fluxes. They are given by

$$L^{uc} = \sum_{ip_b=1}^{2} \left[\left(\sum_{j=1}^{3} \alpha'_{ip_b,j} U_j + \sum_{j=1}^{3} \beta'_{ip_b,j} P_j + \gamma'_{ip_b} \right) (\rho \overline{u} \, \mathrm{d}A_x + \rho \overline{v} \, \mathrm{d}A_y) \right]_{ip_b} \tag{22}$$

$$L^{vc} = \sum_{ip_b=1}^{2} \left[\left(\sum_{j=1}^{3} \alpha''_{ip_b,j} V_j + \sum_{j=1}^{3} \beta''_{ip_b,j} P_j + \gamma''_{ip_b} \right) (\rho \overline{u} \, \mathrm{d}A_x + \rho \overline{v} \, \mathrm{d}A_y) \right]_{ip_b} \tag{23}$$

The coefficients in the above expressions are adequately added to the LHS of x- and y-momentum equations, Equations (18) and (19). The diffusion fluxes are also computed on the two cell faces using the gradients of the finite element shape functions, Equation (11). This consideration yields

$$L^{ud} = -\mu \sum_{ip_b=1}^{2} \left[\sum_{j=1}^{3} \left(\frac{\partial N_j}{\partial x} \mathrm{d}A_x + \frac{\partial N_j}{\partial y} \mathrm{d}A_y \right) U_j \right]_{ip_b} \tag{24}$$

$$L^{vd} = -\mu \sum_{ip_b=1}^{2} \left[\sum_{j=1}^{3} \left(\frac{\partial N_j}{\partial x} \mathrm{d}A_x + \frac{\partial N_j}{\partial y} \mathrm{d}A_y \right) V_j \right]_{ip_b} \tag{25}$$

DOI: 10.1002/fld

The treated diffusive terms are added to the LHS of Equations (18) and (19). Eventually, the pressure terms also need to be treated properly. Since we place the outflow boundary at an arbitrary section, we are not able to enforce either Dirichlet or Neumann conditions to specify pressure at this location. Therefore, the roles of pressure terms are implicitly taken into the formulation without the knowledge of their magnitudes at the boundary. In this regard, the pressure terms are approximated by

$$R^{up} = -\sum_{ip_b=1}^{2} \left(\sum_{j=1}^{3} N_j \overline{P}_j \, \mathrm{d}A_y \right)_{ip_b} \tag{26}$$

$$R^{vp} = -\sum_{ip_b=1}^{2} \left(\sum_{j=1}^{3} N_j \overline{P}_j \, \mathrm{d}A_x \right)_{ip_b} \tag{27}$$

These terms are taken to the RHS of Equations (18) and (19). This treatment considers the implicit role of unknown pressure at the outflow calculation. In practice, one x-momentum equation is sacrificed to specify the pressure magnitude at one arbitrary node in the domain. It should be noted that the specification of such a magnitude is mandatory, otherwise, the pressure field is not fixed. However, this node is not necessarily to be a boundary node.

5. THE RESULTS

The extended formulations, which fully guarantee the conservation laws not only in the interior cells, but also at the outflow boundary cells, are investigated by solving the backward-facing step as a standard test case. This test case is known as a difficult one, which is occasionally truncated to study the newly developed boundary condition treatments. The problem definition used here follows Gartling [16], which will allow the comparison of the computed results. Considering a channel height of H, the step height and downstream channel length are $H/2$ and $30H$, respectively. However, we mainly solve the problem on a shortened domain. The problem is tested at $Re = 800$, which results in two primary and secondary recirculations behind the step. The benchmark computations of the backward-facing step flow at this Reynolds were originally intended for use in a mini-symposium on OBCs as well [6]. It is argued that the flow at this Reynolds number is unsteady and exhibits chaotic behaviour [17]. The flow boundary conditions for the step geometry include the no-slip velocity specifications for all solid surfaces, and a parabolic velocity profile at the inlet given by $U(y) = 1.5 \times U_{\mathrm{mean}}(4y^+)(2 - 4y^+)$ where $0 \leqslant y^+ (= y/H) \leqslant 0.5$.

For the outflow boundary conditions, Gartling [16] considers a parallel flow and a constant total stress normal to the outflow boundary, which, in essence, sets the outflow pressure to zero. Generally speaking, the use of pseudo stress-free condition has been very popular for computations over the entire full channel case. This type of natural boundary condition (i.e. $-p + (\partial u/\partial x)/Re = 0$ and $\partial v/\partial x = 0$) can be readily applied at the outlets sufficiently far from the inlets. Sani and Gresho [6] remark that the natural boundary condition is preferable to the true stress-free condition (i.e. $-p + 2(\partial u/\partial x)/Re = 0$ and $\partial u/\partial y + \partial v/\partial x = 0$) because this type of boundary conditions tends to be too restrictive for most flows, at which all stresses do not necessarily vanish at an outflow boundary. The zero normal gradient condition and the radiation condition are two more types of boundary conditions, which have been successfully employed specially in treating the transient

DOI: 10.1002/fld

problems where vortices must leave the computational domain with minimum distortion [1, 2]. For a steady flow, the latter condition should revert to the former one when the steady condition is approached. Despite their general popularity, Sani and Gresho [6] argue that these conditions may yield ill-posed problem. In our formulation, we fully close the outflow boundary without employing any type of boundary condition. In other words, except for the pressure magnitude, which is adjusted for only one arbitrary node located at the outflow boundary, the rest of boundary cells are fully closed. As was mentioned earlier, this node or point is not necessarily to be on the outflow boundary. It can be an interior node as well; however, we have fixed this magnitude at the outflow boundary in our study. Except this exceptional node, the unknown pressure is specified implicitly via the momentum equations for the rest of cells located at the outflow, see Equations (26) and (27).

It should be mentioned that the accuracy of the extended formulation has been already verified. Therefore, we do not intend to re-verify the accuracy of the original code in treating fully bounded solution domains, see References [11, 12]. References [14, 15, 18] solve the extended backward-facing step problem and show excellent agreement with the benchmark. Nevertheless, the results of the present code are judged to be very accurate in bounded domains. In this work, the validity of the developed boundary conditions is determined by truncating the channel and the original mesh and applying the new formulation at the new synthetic outflow plane. No grid rearrangement was performed when the channel was truncated. Different types of grid can be distributed in the computational domain to guarantee the most accurate solutions when X_{end} is placed at different longitudinal locations. However, we intend to show the accuracy of the formulation using identical grid distributions. Therefore, we perform the current investigations in two stages. At the first stage, we choose a suitable non-uniform grid distribution along the longitudinal direction. The choice of non-uniform grid is quite normal in treating the backward-facing step problem [7, 16, 18]. It is because the flow is almost fully developed in a major part of the duct downstream of the step. That part does not need fine grid considerations. On the other hand, Sani and Gresho [6] specify that no extra fine meshes be used near the outlet, presumably because the effect of the OBC would thereby be limited by local finite difference and finite element approaches. Indeed, the flow complexities mostly exist around the separation zone beside the step. At the second stage, we ignore the above recommendations and follow the grids utilized by Blosch *et al.* [8]. They are uniform coarse grid distributions.

To study the performance of the new formulations, the computational domain downstream of the step is shortened by a few lengths of 6.5, 8.0, 9.5, 11.0 and 16.0. There are different reasons to choose these specific lengths. Blosch *et al.* [8] report their results at the lengths of 8.0 and 16.0. The lengths of 6.5, 8.0 and 9.5 were purposely selected to cut the upper eddy, thus providing the challenge of letting fluid also flow into the domain. The cross-sections at 6.5 and 9.5 intersect the ends of the upper eddy where the tangential velocity components are not small. Additionally, the length of 6.5 is even shorter than 7.0, which was chosen as a test section by the organizers of the OBCs mini-symposium [6]. A short length of either 7.0 or 6.5 can severely test the ability of an OBCs to allow flow to return into the truncated domain. Since the centre of upper vortex is located around 7.5, section 6.5 is a better choice than 7.0 to study the impact of non-zero tangential velocity components. Additionally, section 6.5 is right after the reattachment point of the lower recirculation (~ 6.1). The section at 11.0 is chosen because it is right after the reattachment point (~ 10.5) of the upper eddy. The transversal grid distribution involves 41 uniform nodes. However, the longitudinal distributions are 151, 201, 243, 271, 321 and 351 for $X_{\text{end}} = 6.5$, 8.0, 9.5, 11.0, 16.0 and 30.0 cases, respectively. To achieve a unique grid distribution, firstly we distribute 351

DOI: 10.1002/fld

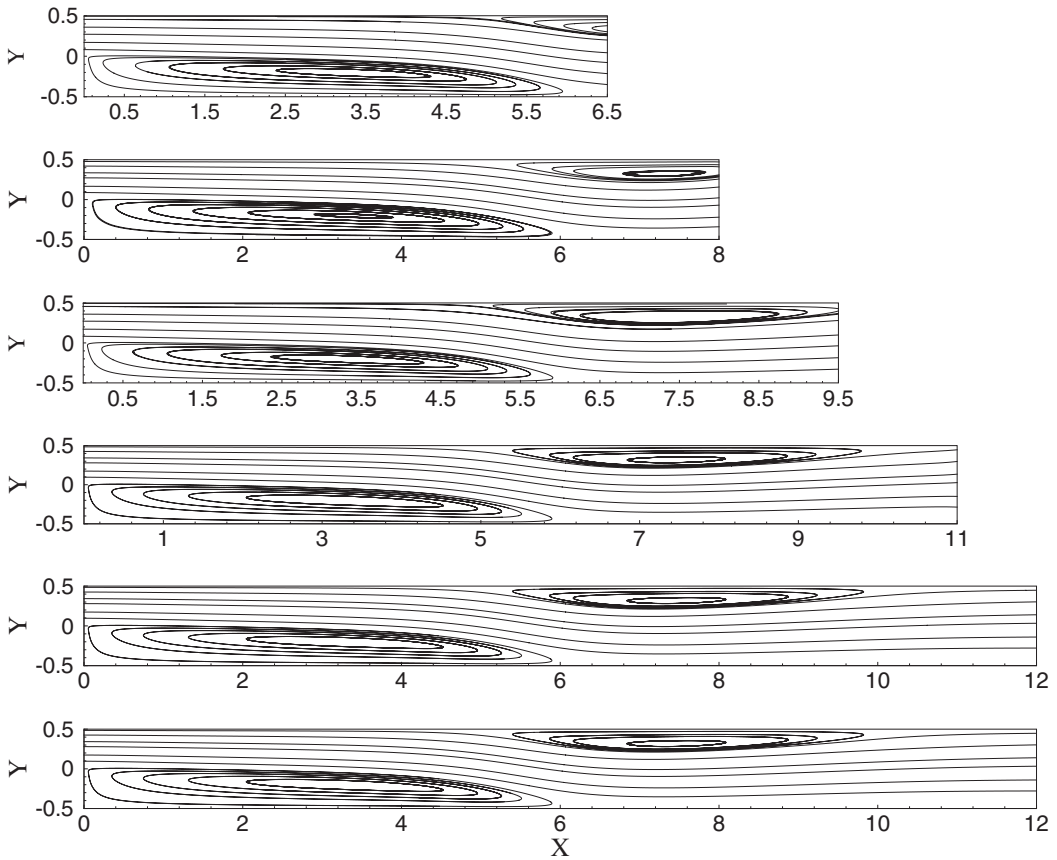

Figure 4. Streamlines in a backward-facing step using a non-uniform grid with $X_{\text{end}} = 6.5$, 8.0, 9.5, 11.0, 16.0 and 30.0 from top to bottom, respectively.

non-uniform nodes in the streamwise direction in the channel with its outlet boundary placed at $X_{\text{end}} = 30$. Secondly, we cut the channel at $X_{\text{end}} = 16.0$, 11.0, 9.5, 8.0 and 6.5 without changing the original distributed grid and solve the flow in the truncated domains. Since the original grid distribution is non-uniform, we name it a non-uniform grid.

Figures 4–6 demonstrate the results obtained using the non-uniform grid. Figure 4 shows the streamlines in the duct. As observed, the qualitative distributions are identical irrespective of placing the outflow at different locations. The outflow section intersects the upper recirculation zone when $X_{\text{end}} = 6.5$, 8.0 and 9.5; however, this cut does not deteriorate the solution even in the vicinity of the outflow sections. Note that Figure 4 only shows the first 24 step heights of the channel since few phenomena of interest occur downstream of this point. Generally speaking, one important factor in solving the step flow problem is to compute the locations of separation and reattachment points on the two upper and lower walls accurately. Considering the worst cut at $X_{\text{end}} = 6.5$, Figure 4 shows that the locations of reattachment point on the lower wall and the separation point on the upper wall are not affected in the truncated domains.

DOI: 10.1002/fld

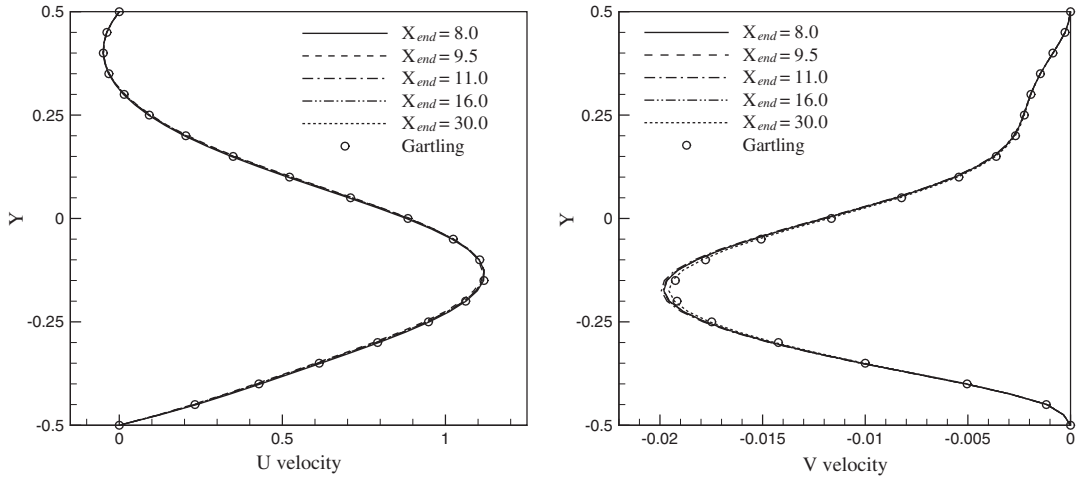

Figure 5. U and V velocity profiles at $x = 7.0$ station using a unique non-uniform grid distribution and considering different X_{end} locations.

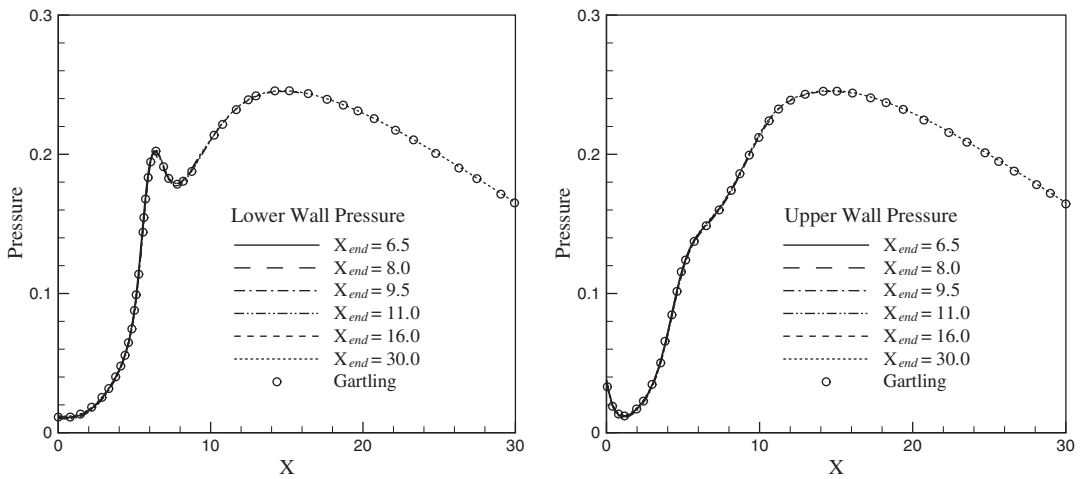

Figure 6. Pressure distribution along the upper and lower walls using a unique non-uniform grid distribution and considering different X_{end} locations.

Figures 5 and 6 quantify the accuracy of the current solutions if the outflow is located at different longitudinal places. Figure 5 demonstrates U and V velocity profiles at $x = 7.0$ station and compares these profiles with those reported by Gartling [16] as the benchmark solution. Similarly, Figure 6 provides the pressure distributions along the lower and upper walls of the channel and compares them with the benchmark results. These two figures indicate that the current algorithm and formulation accurately solve the problem in spite of placing the outflow boundary at different locations even very close to the step. This is in contrast to the results of Behr *et al.* [1],

DOI: 10.1002/fld

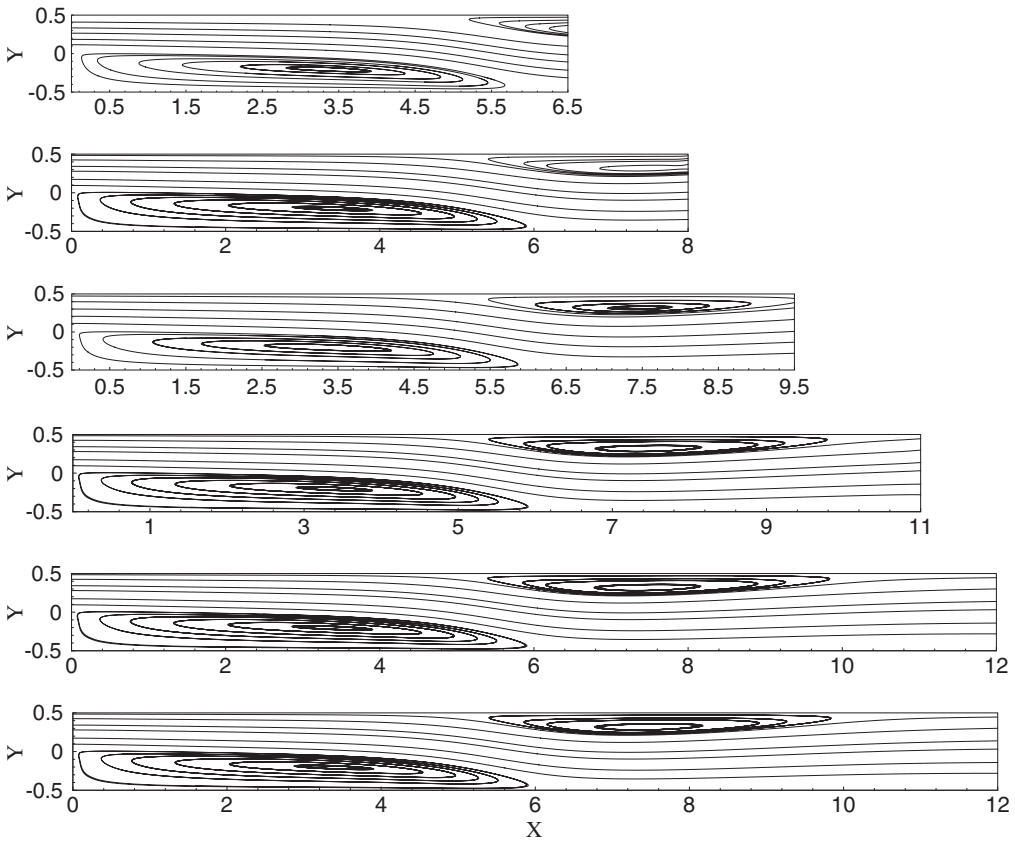

Figure 7. Streamlines in a backward-facing step using a uniform grid with $X_{\text{end}} = 6.5$, 8.0, 9.5, 11.0, 16.0 and 30.0 from top to bottom, respectively.

Sohankar *et al.* [2], and Bao and Xin [19], who show that the solution accuracy can be improved if the location of artificial boundary is moved sufficiently far from the domain of interest.

The second stage of the current investigation focuses on a uniform grid distribution. Following Blosch *et al.* [8], we also choose a coarse uniform grid distribution and ignore the benefits of using a non-uniform grid in the vicinity of the inlet. Therefore, we uniformly distribute 301 nodes in the full-length channel with $X_{\text{end}} = 30.0$. This grid distribution is identical with the distribution presented in Reference [8]. Our anticipation is that the choice of this grid resolution would deteriorate the solution specifically around the recirculation zones and close to the inlet section. This anticipation is normal because of coarsening the grid in the vicinity of the inlet compared with our non-uniform grid utilized at the first stage of this study. Since the grid is uniform, the longitudinal distributions become 301, 161, 111, 96, 81, and 66 when $X_{\text{end}} = 30.0$, 16.0, 11.0, 9.5, 8.0, and 6.5, respectively.

Figure 7 shows the streamlines obtained using the uniform grid distributions. Comparing the streamlines with each other in this figure and with those presented in Figure 4, they indicate that the separation and reattachment points and the streamline patterns are schematically the same

DOI: 10.1002/fld

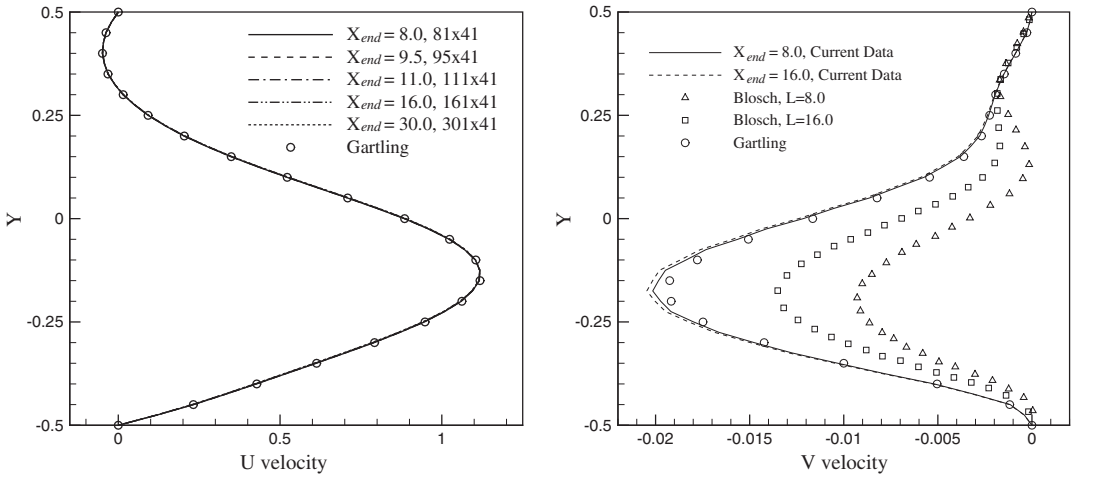

Figure 8. U and V velocity profiles at $x = 7.0$ station using a unique uniform grid distribution with considering different X_{end} locations and a comparison with the available results of Blosch *et al.* [8] at $X_{\text{end}} = 8.0$ and 16.0.

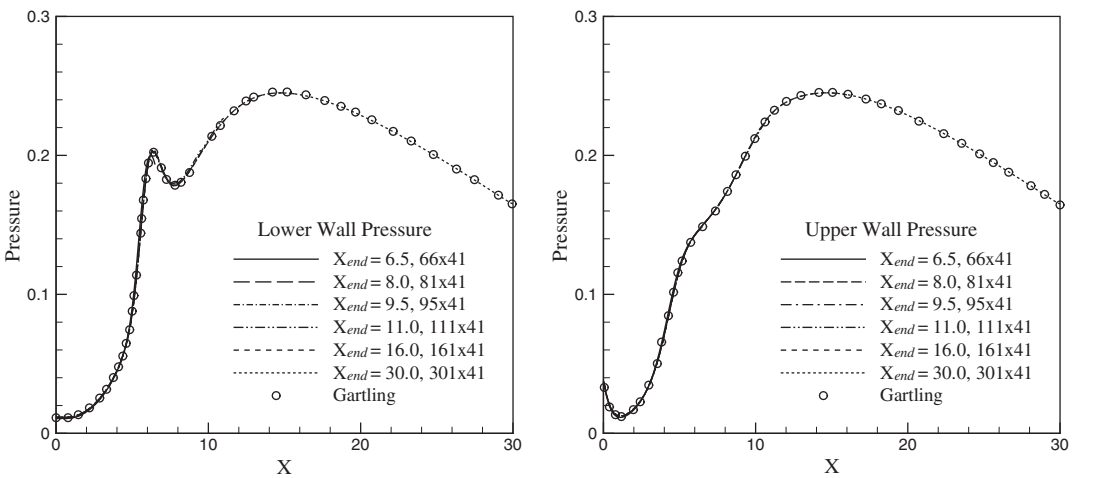

Figure 9. Pressure distributions along the upper and lower walls using a unique uniform grid distribution and considering different X_{end} locations.

irrespective of using uniform grid distributions and placing X_{end} at different longitudinal positions. Comparing Figure 7 with Figure 4, a slight difference is observed at the upper recirculation and close to the outflow section when $X_{\text{end}} = 8.0$. The comparison indicates that the use of a coarse grid close to the inlet may not allow a perfect convergence of the streamlines at the upper face of the outflow section.

Similar to Figures 5 and 6, Figures 8 and 9 show the details of solutions in the channel. Comparing the former figures with the latter ones, it is concluded that the details of solutions

DOI: 10.1002/fld

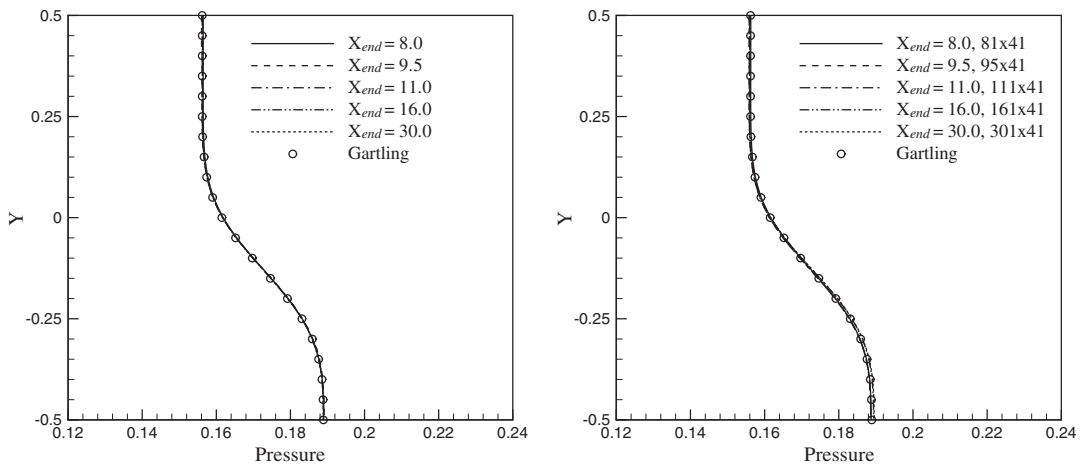

Figure 10. Pressure distribution at $x = 7.0$ station using either a unique non-uniform (left) or a unique uniform (right) grid distributions with different X_{end} locations.

are not altered by switching from a suitable non-uniform grid to a plain uniform grid. On the other hand, comparing the current results with those of benchmark denotes that the achieved accuracies are still excellent despite using uniform coarse grid distributions. As was mentioned, the current grid distribution has been taken from Reference [8]. This reference reports the U and V velocity profiles at $x = 7.0$ station. We use this opportunity and compare our results with those of Blosch *et al.* [8] at this section, see Figure 8. We have not included the U velocity profiles of the reference in this figure because they are in full agreement with that of Gartling. However, their V velocity profiles are not as accurate as ours, see Figure 8 (right). As it is seen, the reference obtains lower values than the Gartling benchmark solutions when placing X_{end} at 8.0 and 16.0 locations. However, the accuracy of the current solution is excellent irrespective of the location of the outflow boundary. There is just a slight difference between the current results and that of benchmark. Reference [14] shows that this slight difference is vanished if the utilized grid is further refined in the vicinity of the inlet, of course, without changing the number of nodes in the longitudinal direction.

To quantify the pressure field more, Figure 10 illustrates the pressure distribution at the critical section of $x = 7.0$ using either non-uniform or uniform grid distributions and compares them with the pressure distributions computed by Gartling [16]. Similar to the preceding figures, the results reemphasize the accuracy of the extended formulation irrespective of the types of grid distribution and the location of outflow boundary.

To compare the efficiency of the current outflow boundary treatment with those of other applicable outflow condition employments, we examine our formulations imposing two other classical non-OBC and OBC cases utilized in the finite volume method. Back to the vast range of OBCs collected in Reference [6], there are two groups, who investigated the truncated backward-facing step using finite volume method. Demuren and Wilson solved the two-dimensional steady equations on a staggered grid. They reported that $\partial V/\partial n = 0$ produced the best results in the sense of minimal sensitivity to computational length and the correct pressure distribution across the outflow for the short-length computations. Similarly, we choose $\partial u/\partial x = 0$ as one class of OBC

DOI: 10.1002/fld

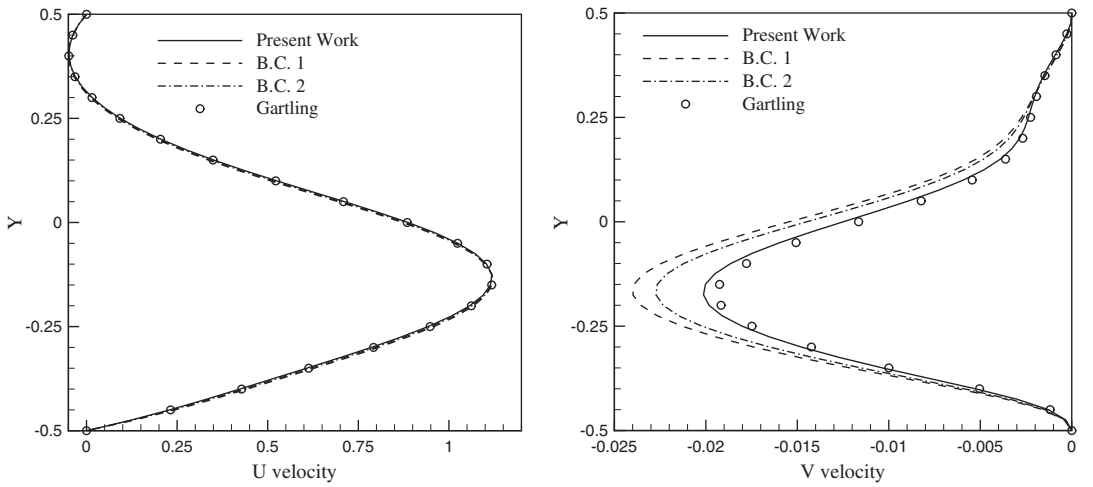

Figure 11. The implementation of two other types of non-OBC and OBC at outflow boundary and comparing their results with those of the current work and benchmark, $x = 7.0$.

to check its efficiency in our formulations. We call it B.C. 1. On the other hand, following the essence of Gartling's outflow boundary condition described in this section and assuming the lack of sufficient knowledge to assess the correct outflow boundary condition employment, we choose incorrect zero pressure at outflow boundary as a non-OBC condition and call it B.C. 2. Figure 11 shows the profiles of longitudinal and transversal velocity components at $x = 7.0$ using these two types of outflow conditions. The results have been compared with those of the current work and Gartling [16]. A few points can be derived here. Firstly, the results have been provided for a truncated domain with $X_{\text{end}} = 8.0$. It is because the results of employing B.C. 1 and B.C. 2 on longer domains were in good agreement with the two other results. It was observed that the differences would become more serious when the outflow section was placed closer to the inlet section. Secondly, contrary to the v velocity profiles, there are negligible differences in u velocity profiles using either B.C. 1 or B.C. 2 at $X_{\text{end}} = 8.0$. Meanwhile, both of them agree well with the benchmark. Thirdly, the efficiency of B.C. 1 with respect to B.C. 2 is not similar when X_{end} is further reduced. Our observations showed that the solution using B.C. 2 would not converge for very short domains.

From the convergence point of view, it is a good question whether the new outflow treatments affect the rate of convergence. Generally speaking, it is quite normal to assume that the displacement of an outflow boundary from a section with known conditions to another section with unknown conditions would slow down the convergence rate. Figure 12 illustrates that the rate of convergence or the residual reduction rate decreases when X_{end} is located farther from the step. The results belong to the uniform grid case, which was investigated in the second stage of the current study. The horizontal coordinate performs the number of iterations. The figure points out that the insertion of the outflow boundary at arbitrary sections with more uncertainties would increase the iterations. However, it should be realized that this increase would not cause an adverse effect on computational cost because there are a few benefits in diminishing the size of global matrix derived in Section 4, i.e. Equations (17)–(19). Since we use sparse matrix solvers to solve the derived system of linear

DOI: 10.1002/fld

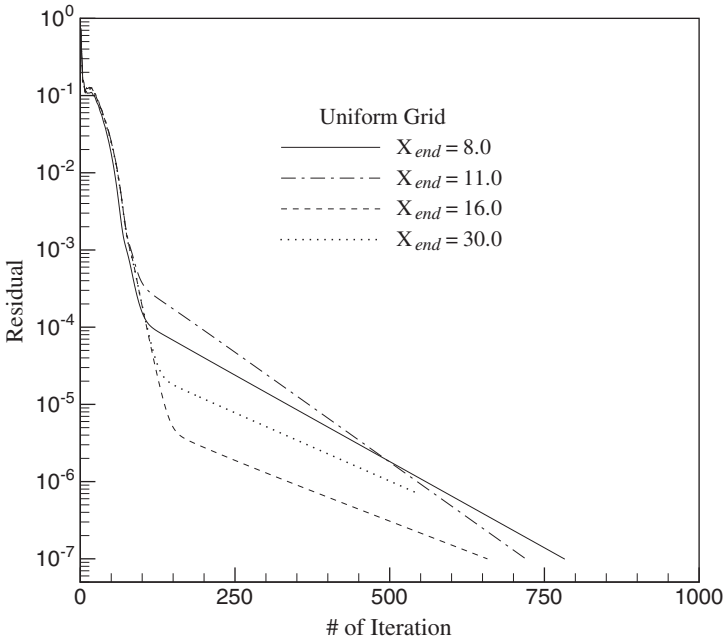

Figure 12. Convergence histories for solving the problem using a unique uniform grid distribution considering different X_{end} locations.

algebraic equations, there is a big reduction in the solution time spent by our sparse solver when the size of constructed matrix of coefficients is relatively reduced.

Although the current formulation has been applied to steady problems, it can be equally applied to solve unsteady problems. Considering the convergence histories of the steady backward-facing step problem presented in Figure 12, some conclusions can be readily derived if the same formulation and algorithm are utilized to solve an unsteady problem. For example, it is easily concluded that if the exit boundary is placed at different chosen locations there would be a little difference in the numbers of cycles to achieve the solution at each time step of a time-dependent solution. As was mentioned in the preceding paragraph, the employment of our improved formulation effectively reduces the computational time if the exit boundary is placed closer to the inlet section. It is because the size of the global matrix derived in each time step is considerably decreased due to the reducing total number of grid nodes in smaller solution domains. However, before using this strategy to solve a time-dependent problem, it is always worth to answer the question whether the use of a fully implicit method to solve an unsteady problem is computationally cost-effective.

6. CONCLUSIONS

A major challenge in the computational fluid dynamics is to reduce the computational cost by diminishing the solution domain sizes. However, this may normally result in solution domains with insufficient information at their artificial boundaries. To overcome the difficulty, an approach, which

DOI: 10.1002/fld

implicitly closes the conservative statements at the boundaries with insufficient information, was introduced. The extended outflow boundary treatment is fully conservative, and implicitly considers the role of unknown pressure field at the outflow. The extended formulation was then investigated by solving the truncated backward-facing step problem with different lengths. The investigation showed that the location of outflow boundary could be arbitrarily changed without adverse effect on the accuracy of the solution. The accuracy of the solution was excellent despite cutting the step at improper longitudinal locations where a recirculation was intersected. Additionally, it was shown that the accuracy of the current solutions was not so sensitive to grid distribution although the step flow problem is known as a mesh-dependent problem. From the computational cost perspective, the new implicit treatment decelerates the convergence rate; however, the computational time does not equally increase because the matrix of coefficients becomes considerably small. The extended formulation is ideal for treating the fluid flow and heat problems with complex boundary behaviours.

REFERENCES

1. Behr M, Hastreiter D, Mittal S, Tezduyar TE. Incompressible flow past a circular cylinder: dependence of the computed flow field on the location of the lateral boundaries. *Computer Methods in Applied Mechanics and Engineering* 1995; **123**:309–316.
2. Sohankar A, Norberg C, Davidson L. Low-Reynolds-number flow around a square cylinder at incidence: study of blockage, onset of vortex shedding and outlet boundary condition. *International Journal for Numerical Methods in Fluids* 1998; **26**:39–56.
3. Griffiths DF. The no boundary condition outflow boundary condition. *International Journal for Numerical Methods in Fluids* 1997; **24**:393–411.
4. Renardy M. Imposing no boundary condition at outflow: why does it work? *International Journal for Numerical Methods in Fluids* 1997; **24**:413–417.
5. Papanastasiou TC, Malamataris N, Ellwood K. A new outflow boundary condition. *International Journal for Numerical Methods in Fluids* 1992; **14**:587–608.
6. Sani RL, Gresho PM. Resume and remarks on the open boundary condition minisymposium. *International Journal for Numerical Methods in Fluids* 1994; **18**:983–1008.
7. Keskar J, Lyn DA. Computations of a laminar backward-facing step flow at $Re = 800$ with a spectral domain decomposition method. *International Journal for Numerical Methods in Fluids* 1999; **29**:411–427.
8. Blosch E, Shyy W, Smith R. The role of mass conservation in pressure-based algorithms. *Numerical Heat Transfer*, *Part B* 1993; **24**:415–429.
9. Darbandi M, Schneider GE. Momentum variable procedure for solving compressible and incompressible flows. *AIAA Journal* 1997; **35**:1801–1805.
10. Darbandi M, Schneider GE. Analogy-based method for solving compressible and incompressible flows. *Journal of Thermophysics and Heat Transfer* 1998; **12**:239–247.
11. Darbandi M, Mazaheri-Body K, Vakilipour S. A pressure-weighted upwind scheme in unstructured finite-element grids. In *Numerical Mathematics and Advanced Applications*, Feistauer M, Dolejsi V, Knobloch P, Najzar K (eds). Springer: New York, 2004; 250–259.
12. Darbandi M, Schneider GE, Vakilipour S. A modified upwind-biased strategy to calculate flow on structured-unstructured grid topologies. *AIAA Paper 2004-0435*, *The 42nd AIAA Aerospace Sciences Meeting and Exhibit*, Reno, 5–8 January 2004.
13. Darbandi M, Naderi AR. Multiblock hybrid grid finite volume method to solve flow in irregular geometries. *Computer Methods in Applied Mechanics and Engineering* 2006, in press.
14. Darbandi M, Schneider GE, Vakilipour S. A full conservative approach to simulate outflow at artificial boundaries. *Proceedings of the 12th Annual Conference of the CFD Society of Canada*; CFDSC, Ottawa, ON, Canada, 2004.
15. Darbandi M, Vakilipour S. Implementation of free boundary condition at arbitrary sections using implicit conservative statements. *Proceedings of the 4th European Congress on Computational Methods in Applied Sciences and Engineering*, *ECCOMAS 2004*, Jyväskylä, Finland, 24–28 July 2004.

DOI: 10.1002/fld

16. Gartling DK. A test problem for outflow boundary conditions—flow over a backward-facing step. *International Journal for Numerical Methods in Fluids* 1990; **11**:953–967.
17. Kaiktsis L, Karniadakis GE, Orszag SA. Onset of three-dimensionality, equilibria, and early transition in flow over a backward-facing step. *Journal of Fluid Mechanics* 1991; **231**:501–528.
18. Darbandi M, Schneider GE. Application of an all-speed flow algorithm to heat transfer problems. *Numerical Heat Transfer*, *Part A* 1999; **35**:695–715.
19. Bao W, Xin W. The artificial boundary conditions for computing the flow around a submerged body. *Computer Methods in Applied Mechanics and Engineering* 2000; **188**:473–482.

DOI: 10.1002/fld